Applied Catalysis B: Environmental 328 (2023) 122543

Contents lists available at ScienceDirect

Applied Catalysis B: Environmental

journal homepage: www.elsevier.com/locate/apcatb

Synthesis of platinum intermetallic nanoparticle fuel cell catalysts within secure inter-particle distance on carbon blacks

Peng Yin [a,b], Lu-Jie Zuo [b], Wei-Jie Zeng [b], Ming Zuo [b], Lei Tong [a,b], Xian-Zhu Fu [a,*], Hai-Wei Liang [b,*]

[a] College of Materials Science and Engineering, Shenzhen University, Shenzhen 518060, China
[b] Hefei National Laboratory for Physical Sciences at the Microscale, Department of Chemistry, University of Science and Technology of China, Hefei 230026, China

ARTICLE INFO

Keywords:
Intermetallics
Oxygen reduction reaction
Fuel cell
Inter-particle distance

ABSTRACT

Supported ordered intermetallic nanoparticles are of significant interest for catalysis applications owing to their unique surface/near-surface structures and electronic properties. However, the synthesis of small-sized intermetallic catalysts with high mass activity remains a formidable challenge, as high temperatures annealing treatments are generally requisite to achieve ordered intermetallic structures but lead to undesired larger crystallites. Here, we report an industrially relevant impregnation approach for the scalable synthesis of small-sized platinum-based intermetallic nanoparticle catalysts by regulating inter-particle distance on carbon black supports to mitigate metal sintering in high-temperature annealing. We construct a library consisting of 18 binary Pt-based intermetallic nanoparticle catalysts with an average size of < 5 nm. The prepared intermetallic catalyst libraries exhibit outstanding proton-exchange-membrane fuel cells performance, including high mass activities of 1.3–1.8 A mg_{Pt}^{-1}, large peak power densities of 1.2–1.4 W cm^{-2} in H_2-air cells, and efficient Pt utilization of ~0.07 g kW^{-1} at rated power.

1. Introduction

Intermetallic compounds (IMCs) have raised sustained research interests in the field of catalysis, as their defined stoichiometry and crystal structure afford intriguing geometric/electronic properties that can promote activity, selectivity, and stability [1–5]. The position of each constituent element in IMCs is determined rather than random, which ensures the homogeneity and reproducibility of active sites in compare to disordered alloys. Moreover, the regular surface atom arrangements enable IMCs with certain molecular recognition ability to adsorb/desorb diverse functional groups, further highlighting the remarkable capability in catalytic performance enhancement [6–8]. For catalyzing the electrochemical oxygen-reduction reaction (ORR) in proton-exchange membrane fuel cells (PEMFCs), ordered IMCs catalysts are distinctly advantageous over their disordered counterparts for enhancing ORR activity because of more pronounced compressive strain effect in IMCs structures [9,10].

According to the principle of phase diagram, the formation of IMCs phases is thermodynamically favorable below phase transition temperature owing to the negative Gibbs' free energy in disorder-to-ordered transition [11]. However, the realization of disorder-to-ordered transition must overcome the energy barrier of atom diffusion and ordering in dynamics. Traditional syntheses of IMCs catalysts are reliant on high-temperature processes (for example, powder metallurgy, arc melting, and induction heating) that promote the atom diffusing and ordering and thereby insure the formation of intermetallic phases [12–14]. These methods unfortunately failed to produce nano-sized intermetallic particles with high surface areas and mass-based activities for practical catalysis applications, even after post-synthesis crushing or ball milling treatments. Some efforts were devoted recently to the synthesis of small sized Pt-based IMCs for electrocatalysis applications [15–18]. The most common anti-sintering strategy in IMC synthesis is protective coating of disordered alloy particles before annealing [19–23], which is essentially a physical barrier that avoids the contact among particles to suppress sintering. Nevertheless, most of these procedures require tedious multistep processes and therefore are difficult to realize the economic and scalable synthesis of IMCs catalysts. Some other strategies, like mitigation of high-temperature sintering based on strong interactions between metal and heteroatom-doped carbons [24,25], are also not suitable for on easily available carbon

* Corresponding authors.
E-mail addresses: xz.fu@szu.edu.cn (X.-Z. Fu), hwliang@ustc.edu.cn (H.-W. Liang).

https://doi.org/10.1016/j.apcatb.2023.122543
Received 18 November 2022; Received in revised form 1 February 2023; Accepted 26 February 2023
Available online 27 February 2023
0926-3373/© 2023 Elsevier B.V. All rights reserved.

blacks for practical fuel cell applications.

Here, we present an industrially relevant wet-impregnation approach for the synthesis of small Pt-based IMCs nanoparticles catalysts by the rational regulation of inter-particle distance on diverse and commercially available carbon black supports. We previously found that prolonging inter-particle distance could effectively suppress the particle coalescence and slow down the Ostwald ripening, and we quantified a critical particle distance over which the sintering could be mitigated significantly up to 900 °C on carbon supports [26]. We apply the critical-particle-distance anti-sintering strategy to the high-temperature synthesis of small sized IMCs catalysts. The maximal IMCs loading is determined on each carbon black supports according to their specific surface area to ensure the secure particle distance, by which the alloy nanoparticles evolve into intermetallic phases in high-temperature annealing but do not suffer from severe sintering. Through this high-temperature secure-particle-distance approach we synthesized 18 kinds of binary Pt-based IMCs catalysts with an average size of < 5 nm. Thanks to the small size with high active surface area, the intermetallic catalyst libraries exhibit outstanding electrocatalytic performance in practical PEMFCs, including high H_2-O_2 fuel cell mass activities of 1.3–1.8 A mg_{Pt}^{-1} at 0.9 V, H_2–air fuel cell peak power densities of 1.2–1.4 W cm^{-2}, high rated power densities of > 1 W cm^{-2} with an efficient Pt utilization of ~ 0.07 g kW^{-1}, as well as only 15 mV loss at 0.8 A cm^{-2} after 30 K square wave accelerated stress test, all of which surpass the US Department of Energy (DOE) 2025 targets.

2. Experimental section

2.1. Materials

Vanadium trichloride (VCl_3) was purchased from Sigma-Aldrich. Scandium chloride ($ScCl_3$) and germanium chloride ($GeCl_4$) were purchased from Alfa Aesar. Indium chloride ($InCl_3$) was purchased from Shanghai Macklin Biochemical Co., Ltd., China. All other chemicals were purchased from Sinopharm Chemical Reagent Co. Ltd., China, including hexachloroplatinic hexahydrate ($H_2PtCl_6{\cdot}6\ H_2O$), aluminium chloride ($AlCl_3$), titanium tetrachloride ($TiCl_4$), chromium chloride hexahydrate ($CrCl_3{\cdot}6\ H_2O$), manganous chloride tetrahydrate ($MnCl_2{\cdot}4\ H_2O$), ferric chloride hexahydrate ($FeCl_3{\cdot}6\ H_2O$), cobalt chloride hexahydrate ($CoCl_2{\cdot}6\ H_2O$), nickel chloride hexahydrate ($NiCl_2{\cdot}6\ H_2O$), copper chloride dihydrate ($CuCl_2{\cdot}2\ H_2O$), Zinc chloride ($ZnCl_2$), gallium nitrate hydrate ($Ga(NO_3)_3{\cdot}nH_2O$), stannous chloride dihydrate ($SnCl_2{\cdot}2\ H_2O$), and ethanol absolute (C_2H_5OH). All the chemicals were used as received without further purification. DI water (18.2 MΩ/cm) used in all experiments was prepared by passing through an ultra-pure purification system.

2.2. Synthesis of Pt intermetallic catalyst libraries

The synthesis of Pt_3Fe IMCs catalyst was first selected as the typical example to demonstrate the identification of secure inter-particle distance on carbon black BP2000. The synthesis involved the wet-impregnation of aqueous solution containing metal salt precursors before high-temperature thermal reduction in 5% H_2/Ar. Briefly, 50 mg BP2000 was dispersed into 50 mL aqueous solution containing a certain amount of $H_2PtCl_6{\cdot}6\ H_2O$ and $FeCl_3{\cdot}6\ H_2O$ with Pt/Fe molar ratio of 3:1, which was then dried with a rotary evaporator. The total nominal metal contents of the catalysts were controlled to be 20, 30, 40, and 50 wt%, respectively. The dried powder precursors were finally subjected to high-temperature H_2-annealing treatment at 900 °C with a heating/cooling rate of 5 ºC min^{-1} to obtain a family of intermetallic Pt_3Fe/BP2000 samples. The average particle sizes of these samples were estimated by XRD and HAADF-STEM analyses to identify the secure inter-particle distance for the synthesis small-sized Pt_3Fe IMCs nanoparticles catalysts. Pt_3Fe IMCs catalysts were also prepared by the identical procedure with total metal content for 10, 15, and 20 wt% for carbon black XC-72R, KJ300J, and KJ600J supports, respectively. The "secure inter-particle distance" was then applied to synthesize the Pt intermetallic catalyst libraries on carbon black BP2000 supports with a total nominal metal content of 20 wt% by similar wet-impregnation and high-temperature H_2-annealing process. The 900°C-2 h is sufficient as a general synthesis condition to form the IMC phase, and it could be optimized for some specific IMC. For the wet-impregnation of Sc, Ti, Ge, and Sn salts, hydrochloric acid was added to prevent hydrolysis. For the synthesis of PtCo and PtNi, two-step H_2-annealing involved a high-temperature alloying stage and a low-temperature ordering stage was adopted. For the synthesis of PtZn, the stepwise impregnation of Zn salts was adopted, in which Pt_3Zn was synthesized firstly, followed with another impregnation/H_2-annealing step to convert Pt_3Zn to PtZn. The optimal synthesis recipes for each IMCs catalyst were summarized in Supplementary Table S1. For the gram-scale synthesis of PtFe IMCs catalyst, the whole synthesis procedure was identical as above, except for expanding the dosage to 0.413 g $H_2PtCl_6{\cdot}6\ H_2O$, 0.28 g $FeCl_3{\cdot}6\ H_2O$, 1 g BP2000, and 500 mL deionized water in the wet-impregnation step.

2.3. PEMFCs tests

Prior to the tests, the catalysts were first stirred in 0.1 M $HClO_4$ at 60 °C for 6 h, followed by annealing under 5% H_2/Ar at 400 °C for 2 h, which obtained Pt-IMC@Pt core/shell catalysts. Before sonication to form a homogeneous ink, catalysts were first dispersed in n-propanol/water (1:1) solvent with D2020® perfluorosulfonic acid (PFSA) ionomer at 0.8 ionomer/carbon ratio. The concentration of the ink was controlled to be 3 $mg_{cat.}$ mL^{-1}. The catalyst-coated-membrane (CCM) was made on GORE Nafion membrane (5 cm^2) using an ultrasonic spray (Siansonic UC320, Siansonic Technology Co., Ltd). A gas diffusion layer (GDL) was used Freudenberg (H24CX483) including a microporous layer. The membrane electrode assembly (MEA) was obtained by two GDLs, two gaskets, and the prepared CCM. Single fuel cell test station was Scribner 850e. Prior to the data collection, an activation was applied as followed. The fuel cell voltage was kept at 0.5 V for 10–15 h until the current density reached a stable value. Then the H_2-O_2 polarization plots were kept scanning to further activation using fuel cell test station in a voltage-scanning mode until a steady state was achieved.

The mass activity (MA) of the IMCs catalyst was measured under H_2-O_2 conditions. The MEA was made with the PtFe/Co/Ni cathode with a Pt loading of around 0.03–0.05 mg_{pt} cm^{-2} and the Pt/C (20 wt%, Johnson Matthey) anode with a Pt loading 0.02 $mg_{pt}cm^{-2}$. We first made the calibration curves to quantify the relationship between the number of spray cycles and catalysts loading on the PTFE substrate. Then the required numbers of spraying cycle for a targeted Pt loading could be calculated. The reproducibility of the instrument ensures the accuracy of each spraying. We measured the MEA mass activity three times to obtain an error bar. Test conditions: 5 cm^2 electrode, 80 ºC, 100% relative humidity, 150 kPa_{abs}, outlet H_2–O_2 at 0.2/0.5 L min^{-1} flow rate. The H_2-O_2 fuel cell was operated at 0.9 $V_{iR\text{-}correct}$ for 15 min and the MA was calculated based on the average current density at the last 1 min. For comparison, the Pt/C cathode with a high Pt loading of ~0.23 mg cm^{-2} was also tested to measure the MA.

For H_2-air single cell test, the PtFe/Co/Ni cathode of MEA was made at a fixed Pt loading of 0.05 mg_{pt} cm^{-2} and the Pt/C anode with a fixed Pt loading 0.02 mg_{pt} cm^{-2}. Test conditions: 5 cm^2 electrode, 80 (or 94) ºC, 100% relative humidity, 150 (or 250) kPa_{abs}, outlet H_2–air at 0.5/2 L min^{-1} flow rate. For comparison, MEA made with Pt/C cathodes with a low (0.04 mg_{pt} cm^{-2}) and high (0.23 mg_{pt} cm^{-2}) were also measured.

The accelerated durability test (ADT) in MEA was carried out using a square wave voltage from 0.6 to 0.95 V with a duration of 3 s at each voltage level, according to the US DOE MEA ADT protocol for PGM-based catalysts. Each test was run up to 30,000 cycles at 80 °C, 100% RH, with H_2/N_2 flow 200/75 sccm for the anode and cathode, respectively. When used the ultrathin GORE membrane (12 μm), we were occasionally unable to get any current at 0.9 V at the end of test owing to

the low open-circuit voltage caused by high hydrogen crossover. Therefore, a thick membrane Nafion 211 (25 μm) was used in the ADT for MA evaluation. This difference has no effect on the mass activity evaluation, because the mass activity was obtained by removing the internal resistance and only focuses on the intrinsic activity of catalysts.

2.4. Characterization

XRD analyses were performanced on a Japan Rigaku DMax-γA rotation anode x-ray diffractometer equipped with graphite monochromatized Cu-K radiation. HAADF-STEM images were produced on FEI Talos F200X operated at 200 kV. Atomic resolution HAADF-STEM images were produced on probe aberration-corrected JEM ARM200F (S) TEM operated at 200 kV. EDS mapping and linear scanning were used FEI Talos F200X equipped with Super X-EDS system (four systematically arranged windowless silicon drift detectors). Mo mesh support film was used to replace Cu support film for the all samples containing Cu elements. Inductively coupled plasma atomic emission spectrometry (ICP-AES) measurements were conducted using an Atom scan Advantage Spectrometer (Thermo Ash Jarrell Corporation).

3. Results and discussion

3.1. Identification of secure inter-particle distance

Fig. 1 schematically illustrates the synthesis small-sized IMCs nanoparticles catalysts at high temperatures by regulating the inter-particle distance to suppress catalyst sintering. When the inter-particle distance is large enough, the cross-contact among particles that tend to migrate under Brownian motion collide at high temperatures is avoided and the sintering is mitigated significantly by completely cut off the sintering path of particle migration and aggregation (Fig. 1a). In contrast, the particles with shorter inter-particle distance would have numerous cross-contact regions with a higher risk of particle sintering (Fig. 1b). A maximal IMCs loading on each carbon support can be determined according to their specific surface area to ensure the secure particle distance for mitigating sintering. The average particle distance can be estimated by assuming the perfectly uniform particle size and equidistant distribution of Pt particles on carbon supports (Eq. 1) [27]:

$$d = \sqrt{\frac{\pi}{3\sqrt{3}} \bullet 10^{-3} \bullet \rho_{pt} \bullet \left(\frac{100 - W_{pt}}{W_{pt}}\right) \bullet A_s \bullet r^3} - r \quad (1)$$

where d, ρ_{pt}, W_{pt}, A_S, and r are average particle distance, density of bulk Pt, Pt loading (%), specific surface area of carbon supports ($m^2\ g^{-1}$), and target particle size (nm), respectively. The above equation was applied on a certain carbon support Black Pearl 2000 (BP2000) with a specific surface area of ~1400 $m^2\ g^{-1}$ to obtain quantitative relations between metal loading, particle size, and average particle distance, as displayed graphically in Fig. 2a. It is roughly seen that the red region with a smaller particle distance has a higher risk of sintering.

To accurately quantify the critical particle distance, we took Pt_3Fe IMCs synthesis via a conventional wet-impregnation/H_2-annealing procedure as an example to obtain a family of samples with varied inter-particle distance by changing the metal loading on BP2000 at 900 °C. We estimated the average crystallite size by the Debye-Scherer equation based on the full-width at half-maximum of X-ray diffraction (XRD) patterns to eliminate the possible illusion caused by the very local electron microscopy observations. Evidently, when the metal loading increased, the Pt_3Fe gradually sintered into large particles (Fig. 2b). At a proper metal loading of ~30 wt%, the average crystallite size of Pt_3Fe IMCs was controlled at a small size of around 4.1 nm. High-angle annular dark-field scanning transmission electron microscopy (HAADF-STEM) images also certified the uniform distribution of the particles without obvious sintering (Fig. S1). But a bimodal particle size distribution of 4.2/8.7 nm appeared for the 40 wt% Pt_3Fe sample as revealed by the overlapped widened/sharp (111) peak in XRD patterns (Fig. 2c). Further increasing the loading to 50 wt%, the (111) peak

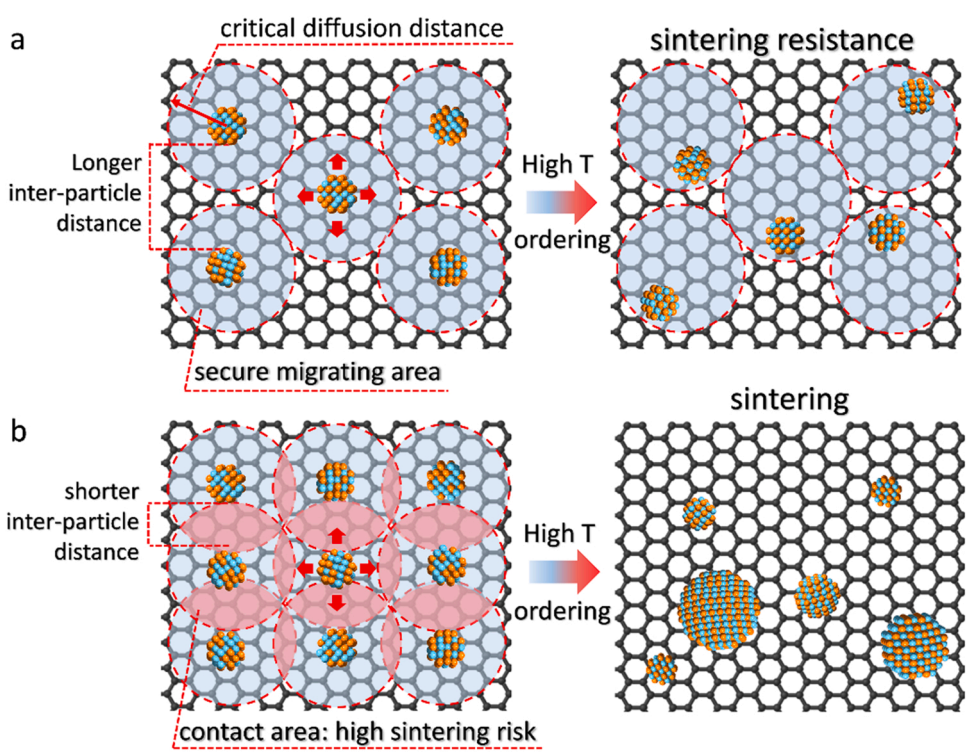

Fig. 1. Schematic illustration of the synthesis of small-sized Pt-based IMCs catalysts within secure inter-particle distance. (a) The particles in secure migrating area have a longer inter-particle distance to avoid sintering during the high-temperature ordering process. (b) The particles with shorter inter-particle distance have more contact possibility to face a high risk of sintering.

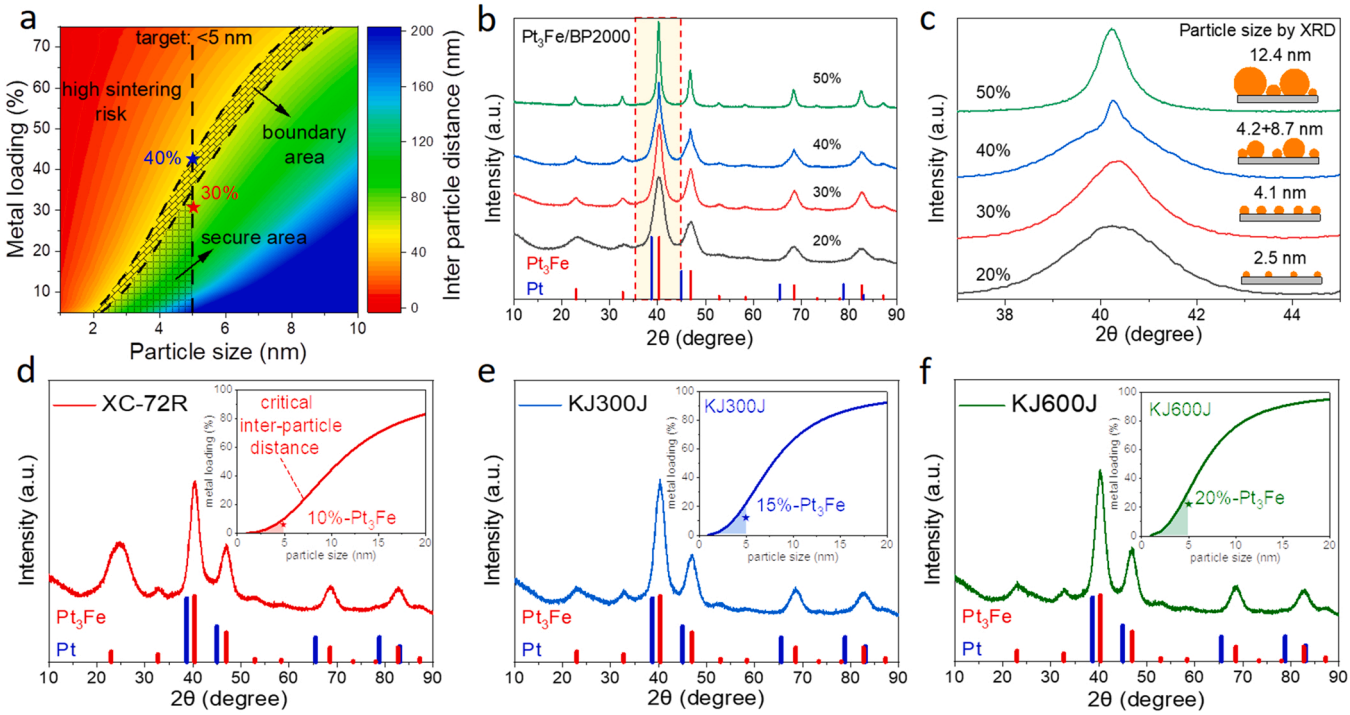

Fig. 2. Quantification of critical inter-particle distance and example proof. (a) Theoretical model prediction of critical inter-particle distance on BP2000 support. The boundary area is the approximate range of the critical inter-particle distance, which is determined by the XRD patterns of Pt_3Fe/BP2000 with varied metal loading shown in (b). (c) The (111) diffraction peaks originate from the magnified region in the yellow box of (b). The insets show the particle size and distribution estimation by XRD results. (d, e, f) XRD patterns of Pt_3Fe IMC supported on XC-72R (d), KJ300J (e), and KJ600J (f) with metal loading of 10, 15, and 20 wt%, respectively. The insets are the critical inter-particle distance curves calculated by specific supports parameters, which facilitate the prediction of secure metal loading.

became very sharp with an average XRD crystallite size of 12.4 nm. HAADF-STEM observations confirmed the particle overgrowth and wide particle size distribution (Fig. S2).

Back to the above relationship diagram shown in Fig. 2a, at a target particle size of < 5 nm, we could predict the critical inter-particle distance to be around 55 nm for the BP2000 supported Pt_3Fe IMCs, corresponding to a metal loading of 30–40% in boundary area (Fig. 2a). Accordingly, the secure area is defined as the enclosed one between the critical particle distance curve and the target size line, in which small-size IMCs with narrow particle size distribution could be synthesized. Instead, the red color area above the critical particle distance curve is high risk in sintering, where IMCs particles tend to sinter into large crystallites.

In principle, similar to BP2000, a critical metal loading could also be identified experimentally for each other carbon black by synthesizing series of samples with varied metal loading. But we could predict the critical metal loading for other supports, as we previously found that there was a close critical particle distance for different carbon blacks [26]. We accordingly adopted 10, 15, and 20 wt% metal loading for Vulcan XC-72R (XC-72R, 250 $m^2\ g^{-1}$), Ketjenblack EC-300 J (KJ300J, 800 $m^2\ g^{-1}$), and Ketjenblack EC-600 J (KJ600J, 1398 $m^2\ g^{-1}$) [26], respectively, to ensure that the inter-particle distance was in the secure area to realize the synthesis of small-sized Pt_3Fe IMCs catalysts (shadow areas in Fig. 2d-f). XRD and HAADF-STEM characterizations validated the synthesis of Pt_3Fe IMCs catalysts with average particle sizes of < 5 nm and narrow particle size distributions (Fig. 2d-f and Figs. S3-S5).

3.2. Synthesis of Pt intermetallic catalyst libraries

To show the powerful and universal ability of the "secure inter-particle distance" concept, we selected carbon black BP2000 that showed a high metal-loading capacity as supports to prepare small-sized Pt-based IMCs catalyst libraries by the industrially relevant impregnation approach. The total nominal metal contents were controlled to be 20 wt% for all the syntheses. The detailed recipe for each IMCs catalyst synthesis was summarized in Supplementary Table 1.

We totally prepared 18 binary Pt-based IMCs on BP2000, including Pt alloyed with early transition metals (Pt_3Sc, Pt_3Ti, Pt_3V, Pt_3Cr), late transition metals (Pt_3Mn, PtMn, Pt_3Fe, PtFe, Pt_3Co, PtCo, PtNi, PtCu, PtZn), group IIIA metals (Pt_3Al, Pt_3Ga, Pt_3In), and group IVA metals (Pt_3Ge and Pt_3Sn). For the synthesis of PtCo and PtNi IMCs, a two-step annealing protocol involving a low-temperature-annealing stage with a prolonged time was adopted to improve the ordering degree [24]. The stepwise impregnation of Zn salts was adopted for the synthesis of PtZn IMCs catalyst, in which Pt_3Zn was synthesized firstly, followed with another impregnation/H_2-annealing step to convert Pt_3Zn to PtZn (Fig. S6).

The diffraction peaks of XRD patterns for all the samples matched perfectly with the standard Powder Diffraction File (PDF) Cards of corresponding IMCs structures (Fig. 3a and Fig. S7). The crystalline structures of these IMCs are classified into i) face-centered-cubic (fcc) structure in space group Pm-3 m including all the Pt_3M-type IMCs (M represents base metal element) except Pt_3Ge, ii) face-centered tetragonal (fct) structure in space group P4/mmm including all the PtM-type IMCs except PtCu, iii) tetragonal structure in space group I4/mcm (Pt_3Ge), and iv) hexagonal structure in space group R-3 m (PtCu). As different metals have changed sintering rate, the final particle size of all Pt-IMCs may be different. According to the semi-empirical *Tamman* temperatures, metals with low melting point may exhibit higher sintering rate with larger particle size. Notably, the average crystallite sizes calculated by the Debye-Scherer equation based on the full-width at half-maximum of XRD patterns were all less than 5 nm (Fig. S8 and Supplementary Table 1).

HAADF-STEM images showed that all IMCs nanoparticles

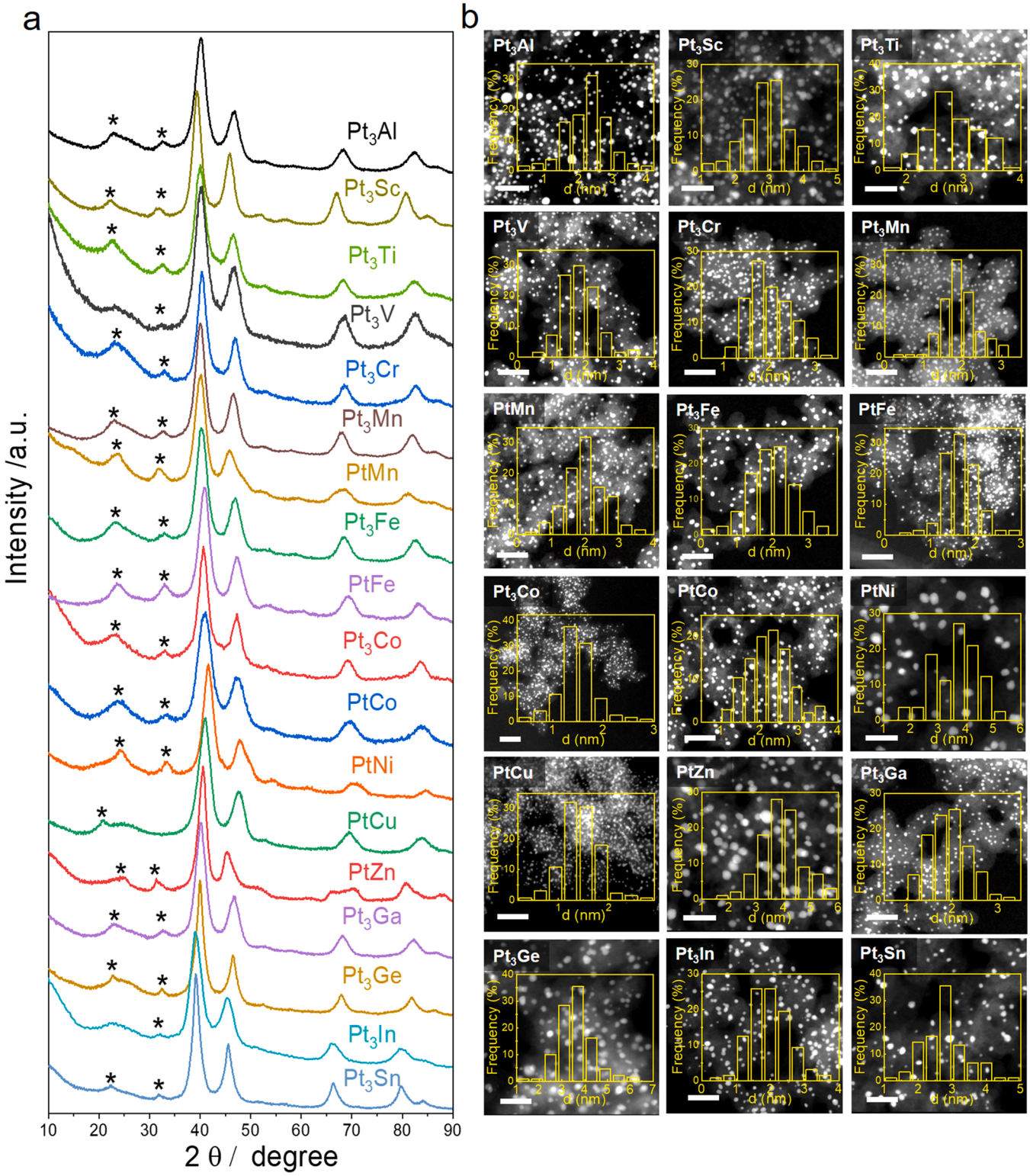

Fig. 3. Synthesis of small-sized IMCs particle catalyst libraries. (a) XRD patterns and (b) HAADF-STEM images of Pt-based IMCs particle catalysts supported on BP2000 with a total metal content of 20 wt%. Asterisks marked in (a) are the characteristic super-lattice peaks of ordered intermetallic structures. Inserted histograms in (b) are the statistics of particle size distribution. Scale bar: 20 nm.

homogeneously distributed over the whole carbon matrix; no obvious aggregates or overgrowth of IMCs nanoparticles were found (Fig. 3b and Figs. S9-S26). Statistical analyses suggested a narrow particle size distribution with average particle sizes of less than 5 nm for all the IMCs samples (Fig. 3b and Supplementary Table S1). Note that the STEM particle sizes are slightly smaller than the values estimated by XRD, as the volume-weighted measurement nature of XRD overestimates the geometric particle size [28]. Further, energy dispersive spectroscopy (EDS) elemental mapping and line scans analyses suggested the homogeneous distributions of Pt and non-Pt elements in individual nanoparticles without element segregation (Fig. 4a and Figs. S27–S35).

We then performed aberration-corrected HAADF-STEM to verify the

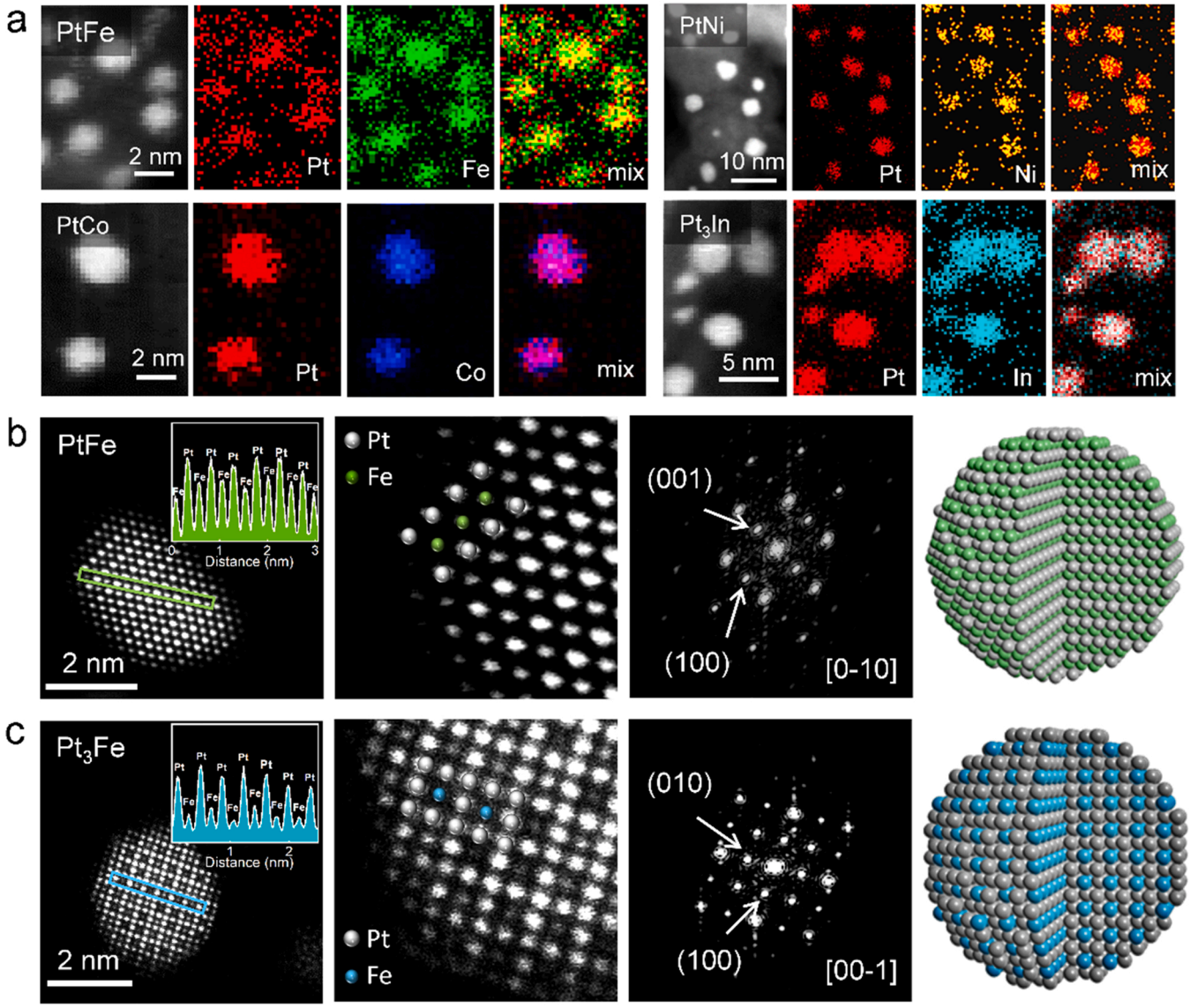

Fig. 4. Structure characterization. (a) EDS elemental mappings of the PtFe and PtCo IMCs catalysts. (b, c) Atomic-resolution HAADF-STEM images, intensity profiles, FFT patterns, and structural models of PtFe (b) and Pt_3Fe (c) IMCs catalysts. PtFe and Pt_3Fe are the CuAu- and $AuCu_3$-type intermetallic structures, respectively.

ordered structure of the IMCs catalysts in atomic scale (Fig. 4b, c). The periodic oscillation of intensity was derived form a column of atoms, which can be attributed to the atomic number (*Z*)-contrast differences between Pt and another metal in an ordered lattice. The Pt atoms will appear brighter than the non-Pt atoms with lower Z. By distinguishing elements from their Z-contrast and measuring the distance between the columns, certain unit cell orientations of the crystal structure were identified. For example, for the case of PtFe IMCs, we observed an alternating bright and dark stacking of Pt and Fe columns along the [1–10] zone axis, which can be assigned to the $L1_0$ ordered structure. While the $L1_2$ ordered structure like Pt_3Fe displayed a structure of a periodic square array of Fe columns surrounded by Pt columns at the edges and corners of each unit cell along the [001] zone axis. Similar atom arrangements were also observed in other $L1_2$ IMCs (Figs. S36-S38). Fast Fourier transform (FFT) patterns further confirmed the order structures of these IMCs catalysts.

3.3. PEMFCs performance

We selected three $L1_0$-type PtM (M = Fe, Co, or Ni) IMCs catalysts for preparing cathodes in membrane electrode assembly (MEA) to evaluate the PEMFCs performance. Prior to PEMFCs tests, the pristine IMCs catalysts were subjected to acid leaching and low-temperature H_2-annealing to form active and stable Pt-IMCs@Pt core-shell structures (Fig. S39) [29–33]. The Pt-IMCs core inside strongly affect the electronic properties of the outside Pt-shell owing to the well-known ligand and/or strain effects[10,29,34–38], which results in a weaker adsorbate bonding to oxygen-containing intermediates and eventually promotes the ORR kinetics with outstanding performance in RDE test (Fig. S40) [39]. Moreover, the Pt-shell could effectively stabilize M against leaching under harsh fuel cell conditions[32,40]: the leached M cations would contaminate the perfluorosulfonic acid (PFSA) ionomers in the catalyst layer of cathode and degrade the transport of protons to the catalytic sites significantly[41,42].

We next tested a series of PEMFCs performance metrics following the US Department of Energy (DOE) guidelines [42,43]. The mass activity (MA) of the catalysts was evaluated in MEA at 0.9 $V_{iR\text{-}correct}$ in the H_2/O_2 tests. Impressively, the IMCs catalysts exhibited high MA of 1.45, 1.80, and 1.78 A mg_{Pt}^{-1} for PtFe, PtCo, and PtNi, respectively (Fig. 5a and Fig. S41), which are 4–6 times that of the benchmark Pt/C catalyst

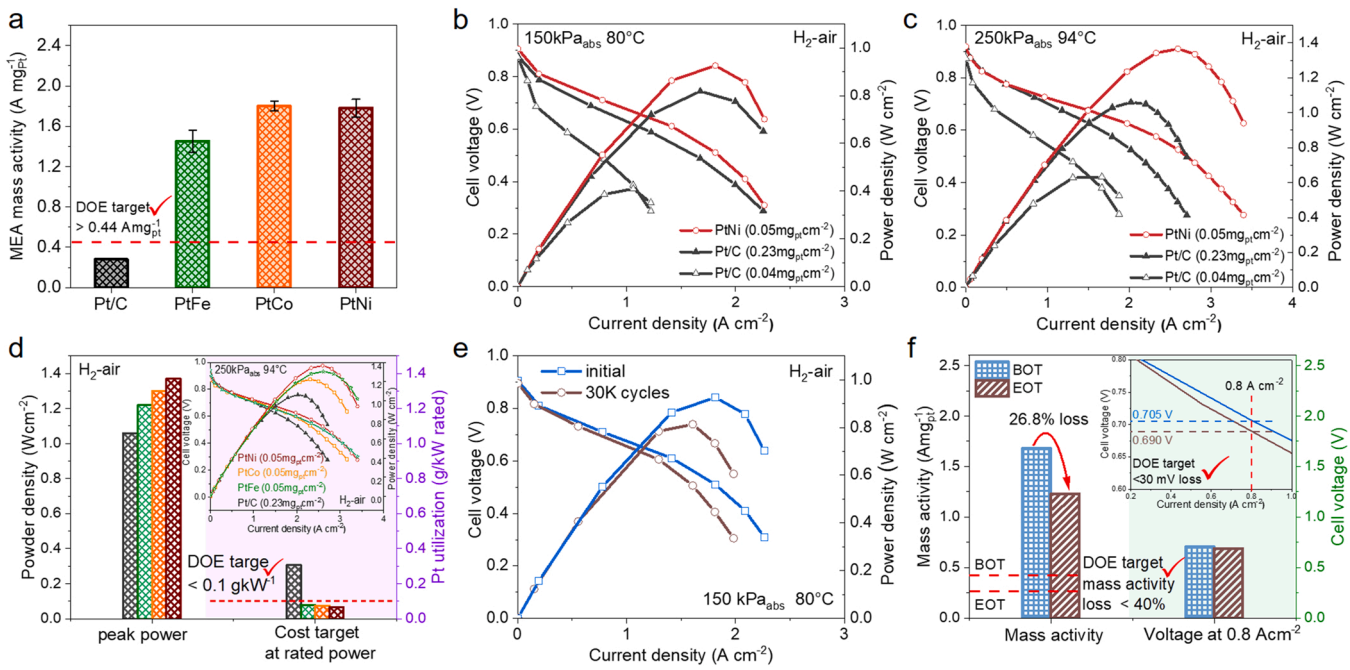

Fig. 5. Fuel cell performance. (a) MEA mass activities in H_2-O_2 test of PtFe, PtCo, PtNi, and Pt/C. Test conditions: 80 °C, 100% relative humidity, 150 kPa_{abs}. (b, c) H_2/air polarization plots/power density plots under 100% relative humidity, 150 kPa_{abs}, 80 °C (b) and 250 kPa_{abs}, 94 °C (c). The anode catalyst is Pt/C, with a loading of 0.02 mg_{Pt} cm^{-2} for all MEAs. (d) Peak power and cost target of PtFe, PtCo, PtNi, and Pt/C at rated power. The insets are the H_2/air polarization plots/power density plots. Test conditions: 94 °C, 100% relative humidity, 250 kPa_{abs}. (e) H_2/air polarization plots/power density plots before and after 30 K square wave ADT. (f) The loss of mass activity and voltage at 0.8 A cm^{-2} after 30 K square wave ADT.

(0.28 A mg_{Pt}^{-1}) and also much exceed the DOE target for MA (0.44 A mg_{Pt}^{-1}), representing the state-of-the-art MA for Pt-based ORR catalysts in MEA tests to date (Fig. S42 and Supplementary Table S2). The high MA was attributed to the combination of high specific activity induced by a strained Pt surface in the ordered Pt-M@Pt core/shell structure [24] and high active surface area resulting from small particle size.

We further evaluate the practical fuel cell performance of the PtM IMCs catalysts under H_2-air conditions. A low Pt loading of 0.05 mg_{pt} cm^{-2} was adopted for the PtM IMCs cathode to meet the DOE target of total Platinum group metal (PGM) loading (0.125 mg_{PGM} cm^{-2}). For comparison, commercial Pt/C was also tested as the cathode catalyst with a low (0.04 mg_{pt} cm^{-2}) and a high (0.23 mg_{pt} cm^{-2}) loading. Commercial Pt/C was used as anode catalysts with a loading of 0.02 mg_{pt} cm^{-2} in all MEA. From the current/power polarization plots under different back-pressure/temperature conditions (150 kPa_{abs}/80 °C or 250 kPa_{abs}/94 °C), we found that the performance of PtM IMCs cathode was significantly better than that of Pt/C cathode at a similar low-Pt loading, and even favorably comparable to that of Pt/C cathode at a 4.6 times higher of Pt loading (0.23 mg_{pt} cm^{-2}) (Fig. 5b,c and Fig. S43). Encouragingly, the low-Pt-loading IMCs cathodes displayed high peak power densities of 1.22–1.37 W cm^{-2}, which were higher than that of high-Pt-loading Pt/C cathode (1.06 W cm^{-2}) (Fig. 5d). We also tested the PtFe IMCs catalyst synthesized in gram-scale, similar high H_2-air fuel cell performance could be achieved, including the peak power densities of 0.9 and 1.2 W cm^{-2} at 150 kPa_{abs}/80 °C and 250 kPa_{abs}/94 °C conditions, respectively (Fig. S44), showing the promising competitiveness of the IMCs catalysts for industrial applications.

For the rated voltage of 0.67 V when the operating temperature is 94 °C, the low-Pt-loading PtFe, PtCo, and PtNi cathodes delivered a rated power density of 0.90, 0.94, and 1.04 W cm^{-2}, respectively, which were higher than that of the high-Pt-loading Pt/C cathode (0.81 W cm^{-2}). After normalized by the total cathode/anode Pt loading, the MEA made with PtM IMCs cathode showed an unprecedented Pt utilization efficiency of 0.067–0.077 g_{Pt} kW^{-1}, which surpassed the cathode made with Pt/C (0.305 g_{Pt} kW^{-1}) as well as the DOE 2025 target (<0.1 g_{PGM} kW^{-1}) (Fig. 5d).

We contributed the superior H_2-air fuel cell performance of the PtM IMCs catalysts to their high MA and small size. The high MA could promote the sluggish O_2 reduction kinetics and thus reduce the cathode overpotential. Besides, it has been widely believed that additional performance loss beyond those predicted by traditional Butler–Volmer kinetics emerged at high current density, which is associated to local O_2 transport resistance through the ionomer film covering the Pt surface [44]. As the O_2 resistance is inversely proportional to the roughness factor (units of cm_{Pt}^2/cm_{MEA}^2) [43,45], the high active surface area of the PtM IMCs catalysts is helpful in minimizing mass-transport losses and achieving high power densities.

We finally evaluated the durability of the MEA made with PtNi cathode by a standard accelerated durability test (ADT) protocol suggested by DOE, in which a square wave potential cycling between 0.60 and 0.95 V (3-second hold at each voltage) was applied to accelerate catalyst degradation, similar to an automotive drive cycle (Fig. 5e and Fig. S45). After 30,000 cycles' ADT, the MA of PtNi IMCs catalyst degraded from 1.68 A mg_{Pt}^{-1} at the beginning of test (BOT) to 1.23 A mg_{Pt}^{-1} at the end of test (EOT), corresponding to a MA loss of by 26.8% (Fig. S46), which exceeded the DOE target (less than 40% loss with an BOT MA of 0.44 A mg_{Pt}^{-1}). Furthermore, the MEA made with PtNi IMCs cathode only showed a voltage drop of ~15 mV at 0.8 A cm^{-2}, which was also meet the DOE target (< 30 mV loss) well and better than commercial Pt/C (~170 mV) (Fig. 5f and Fig. S47).

4. Conclusion

In summary, we present a secure-particle-distance anti-sintering approach to realize the economic and scalable synthesis of libraries of small-sized Pt-based IMCs nanoparticle catalysts on diverse commercial carbon black supports. The key of the synthesis is to control the inter-particles distance to be above a critical value by finely tuning the metal loading on each carbon black support, through which the sintering of metal particles could be significantly mitigated in high-temperature

synthesis. The IMCs catalyst libraries exhibited high peak power densities of 1.2–1.4 W cm^{-2}, large Pt utilization of ~ 0.07 g_{Pt} kW^{-1}, and outstanding durability in practical H_2-air fuel cells. The combinatorial synthesis of intermetallic catalyst libraries spanning a wide range of metal elements allows a comprehensive study of structure-activity relationship in a systematic manner for a variety of energy/chemical-conversion-related reactions.

CRediT authorship contribution statement

Peng Yin: Data curation, Methodology, Writing – original draft, Investigation, Conceptualization. **Lu-Jie Zuo and Wei-Jie Zeng:** Software, Validation. **Ming Zuo:** Software, Visualization. **Lei Tong:** Investigation. **Hai-Wei Liang and Xian-Zhu Fu:** Funding acquisition, Project administration, Conceptualization, Supervision, Validation, Writing – review & editing.

Declaration of Competing Interest

The authors declare that they have no known competing financial interests or personal relationships that could have appeared to influence the work reported in this paper.

Data availability

Data will be made available on request.

Acknowledgements

We acknowledge the funding support from the National Natural Science Foundation of China (Grants 22221003 and 22071225), the National Key Research and Development Program of China (Grant 2018YFA0702001), the Plan for Anhui Major Provincial Science & Technology Project (Grants 202203a0520013 and 202103a05020015), the Fundamental Research Funds for the Central Universities (Grant WK2060190103), the Collaborative Innovation Program of Hefei Science Center of CAS (Grant 2021HSC-CIP015), the China Postdoctoral Science Foundation (Grant 2022M722195) and the Shenzhen Science and Technology Program (Grant JCYJ20200109110416441).

Appendix A. Supporting information

Supplementary data associated with this article can be found in the online version at doi:10.1016/j.apcatb.2023.122543.

References

[1] E. Antolini, Alloy vs. intermetallic compounds: effect of the ordering on the electrocatalytic activity for oxygen reduction and the stability of low temperature fuel cell catalysts, Appl. Catal. B-Environ. 217 (2017) 201–213.
[2] S. Furukawa, T. Komatsu, Intermetallic compounds: promising inorganic materials for well-structured and electronically modified reaction environments for efficient catalysis, ACS Catal. 7 (2017) 735–765.
[3] J. Li, S. Sun, Intermetallic nanoparticles: synthetic control and their enhanced electrocatalysis, Acc. Chem. Res. 52 (2019) 2015–2025.
[4] W. Xiao, W. Lei, M. Gong, H.L. Xin, D. Wang, Recent advances of structurally ordered intermetallic nanoparticles for electrocatalysis, ACS Catal. (2018) 3237–3256.
[5] L. Rößner, M. Armbrüster, Electrochemical energy conversion on intermetallic compounds: a review, ACS Catal. (2019) 2018–2062.
[6] M. Miyazaki, S. Furukawa, T. Komatsu, Regio- and chemoselective hydrogenation of dienes to monoenes governed by a well-structured bimetallic surface, J. Am. Chem. Soc. 139 (2017) 18231–18239.
[7] M. Armbruester, K. Kovnir, M. Behrens, D. Teschner, Y. Grin, R. Schloegl, Pd-Ga intermetallic compounds as highly selective semihydrogenation catalysts, J. Am. Chem. Soc. 132 (2010) 14745–14747.
[8] A. Dasgupta, H. He, R. Gong, S.-L. Shang, E.K. Zimmerer, R.J. Meyer, Z.-K. Liu, M. J. Janik, R.M. Rioux, Atomic control of active-site ensembles in ordered alloys to enhance hydrogenation selectivity, Nat. Chem. 14 (2022) 523–529.
[9] J. Li, S. Sharma, K. Wei, Z. Chen, D. Morris, H. Lin, C. Zeng, M. Chi, Z. Yin, M. Muzzio, M. Shen, P. Zhang, A.A. Peterson, S. Sun, Anisotropic strain tuning of L10 ternary nanoparticles for oxygen reduction, J. Am. Chem. Soc. 142 (2020) 19209–19216.
[10] L. Bu, N. Zhang, S. Guo, X. Zhang, J. Li, J. Yao, T. Wu, G. Lu, J.-Y. Ma, D. Su, X. Huang, Biaxially strained PtPb/Pt core/shell nanoplate boosts oxygen reduction catalysis, Science 354 (2016) 1410–1414.
[11] Y. Yan, J.S. Du, K.D. Gilroy, D. Yang, Y. Xia, H. Zhang, Intermetallic nanocrystals: syntheses and catalytic applications, Adv. Mater. 29 (2017) 1605997.
[12] A.P. Tsai, S. Kameoka, K. Nozawa, M. Shimoda, Y. Ishii, Intermetallic: a pseudoelement for catalysis, Acc. Chem. Res. 50 (2017) 2879–2885.
[13] J. Osswald, R. Giedigkeit, R.E. Jentoft, M. Armbruester, F. Girgsdies, K. Kovnir, T. Ressler, Y. Grin, R. Schloegl, Palladium-gallium intermetallic compounds for the selective hydrogenation of acetylene - Part I: preparation and structural investigation under reaction conditions, J. Catal. 258 (2008) 210–218.
[14] M. Armbruster, K. Kovnir, M. Friedrich, D. Teschner, G. Wowsnick, M. Hahne, P. Gille, L. Szentmiklosi, M. Feuerbacher, M. Heggen, F. Girgsdies, D. Rosenthal, R. Schlogl, Y. Grin, Al13Fe4 as a low-cost alternative for palladium in heterogeneous hydrogenation, Nat. Mater. 11 (2012) 690–693.
[15] D.L. Wang, H.L.L. Xin, R. Hovden, H.S. Wang, Y.C. Yu, D.A. Muller, F.J. DiSalvo, H. D. Abruna, Structurally ordered intermetallic platinum-cobalt core-shell nanoparticles with enhanced activity and stability as oxygen reduction electrocatalysts, Nat. Mater. 12 (2013) 81–87.
[16] Y. Xiong, Y. Yang, H. Joress, E. Padgett, U. Gupta, V. Yarlagadda, D.N. Agyeman-Budu, X. Huang, T.E. Moylan, R. Zeng, A. Kongkanand, F.A. Escobedo, J.D. Brock, F.J. DiSalvo, D.A. Muller, H.D. Abruña, Revealing the atomic ordering of binary intermetallics using in situ heating techniques at multilength scales, P. Natl. Acad. Sci. USA 116 (2019) 1974–1983.
[17] M. Gatalo, M. Bele, F. Ruiz-Zepeda, E. Šest, M. Šala, A.R. Kamšek, N. Maselj, T. Galun, N. Hodnik, M. Gaberšček, A double-passivation water-based galvanic displacement method for reproducible gram-scale production of high-performance platinum-alloy electrocatalysts, Angew. Chem. Int. Ed. 131 (2019) 13400–13404.
[18] H. Cheng, R. Gui, H. Yu, C. Wang, S. Liu, H. Liu, T. Zhou, N. Zhang, X. Zheng, W. Chu, Y. Lin, H. Wu, C. Wu, Y. Xie, Subsize Pt-based intermetallic compound enables long-term cyclic mass activity for fuel-cell oxygen reduction, P. Natl. Acad. Sci. USA 118 (2021), e2104026118.
[19] D.Y. Chung, S.W. Jun, G. Yoon, S.G. Kwon, D.Y. Shin, P. Seo, J.M. Yoo, H. Shin, Y.-H. Chung, H. Kim, B.S. Mun, K.-S. Lee, N.-S. Lee, S.J. Yoo, D.-H. Lim, K. Kang, Y.-E. Sung, T. Hyeon, Highly durable and active PtFe nanocatalyst for electrochemical oxygen reduction reaction, J. Am. Chem. Soc. 137 (2015) 15478–15485.
[20] X.X. Du, Y. He, X.X. Wang, J.N. Wang, Fine-grained and fully ordered intermetallic PtFe catalysts with largely enhanced catalytic activity and durability, Energ. Environ. Sci. 9 (2016) 2623–2632.
[21] Z. Qi, C. Xiao, C. Liu, T.W. Goh, L. Zhou, R. Maligal-Ganesh, Y. Pei, X. Li, L. A. Curtiss, W. Huang, Sub-4 nm PtZn intermetallic nanoparticles for enhanced mass and specific activities in catalytic electrooxidation reaction, J. Am. Chem. Soc. 139 (2017) 4762–4768.
[22] J. Kim, Y. Lee, S. Sun, Structurally ordered FePt nanoparticles and their enhanced catalysis for oxygen reduction reaction, J. Am. Chem. Soc. 132 (2010) 4996–4997.
[23] J. Liang, N. Li, Z. Zhao, L. Ma, X. Wang, S. Li, X. Liu, T. Wang, Y. Du, G. Lu, Tungsten-doped L10–PtCo ultrasmall nanoparticles as a high-performance fuel cell cathode, Angew. Chem. Int. Ed. 131 (2019) 15617–15623.
[24] C.-L. Yang, L.-N. Wang, P. Yin, J. Liu, M.-X. Chen, Q.-Q. Yan, Z.-S. Wang, S.-L. Xu, S.-Q. Chu, C. Cui, H. Ju, J. Zhu, Y. Lin, J. Shui, H.-W. Liang, Sulfur-anchoring synthesis of platinum intermetallic nanoparticle catalysts for fuel cells, Science 374 (2021) 459–464.
[25] J.S. Spendelow, Advanced Electrocatalysts through Crystallographic Enhancement ⟨https://www.energy.gov/sites/prod/files/2019/08/f65/fcto_webinarslides_spendelow_073119.pdf⟩, (2019).
[26] P. Yin, S. Hu, K. Qian, Z. Wei, L.-L. Zhang, Y. Lin, W. Huang, H. Xiong, W.-X. Li, H.-W. Liang, Quantification of critical particle distance for mitigating catalyst sintering, Nat. Commun. 12 (2021) 4865.
[27] J.C. Meier, C. Galeano, I. Katsounaros, J. Witte, H.J. Bongard, A.A. Topalov, C. Baldizzone, S. Mezzavilla, F. Schüth, K.J.J. Mayrhofer, Design criteria for stable Pt/C fuel cell catalysts, Beilstein J. Nanotech. 5 (2014) 44–67.
[28] B.E. Warren, X-ray Diffraction, Courier Corporation, 1990.
[29] P. Strasser, S. Koh, T. Anniyev, J. Greeley, K. More, C.F. Yu, Z.C. Liu, S. Kaya, D. Nordlund, H. Ogasawara, M.F. Toney, A. Nilsson, Lattice-strain control of the activity in dealloyed core-shell fuel cell catalysts, Nat. Chem. 2 (2010) 454–460.
[30] S. Chen, P.J. Ferreira, W.C. Sheng, N. Yabuuchi, L.F. Allard, Y. Shao-Horn, Enhanced activity for oxygen reduction reaction on "Pt(3)CO" nanoparticles: direct evidence of percolated and sandwich-segregation structures, J. Am. Chem. Soc. 130 (2008) 13818–13819.
[31] B.H. Han, C.E. Carlton, A. Kongkanand, R.S. Kukreja, B.R. Theobald, L. Gan, R. O'Malley, P. Strasser, F.T. Wagner, Y. Shao-Horn, Record activity and stability of dealloyed bimetallic catalysts for proton exchange membrane fuel cells, Energ. Environ. Sci. 8 (2015) 258–266.
[32] J. Li, Z. Xi, Y.-T. Pan, J.S. Spendelow, P.N. Duchesne, D. Su, Q. Li, C. Yu, Z. Yin, B. Shen, Y.S. Kim, P. Zhang, S. Sun, Fe Stabilization by intermetallic L10-FePt and Pt catalysis enhancement in L10-FePt/Pt nanoparticles for efficient oxygen reduction reaction in fuel cells, J. Am. Chem. Soc. 140 (2018) 2926–2932.
[33] X. Tian, X. Zhao, Y.-Q. Su, L. Wang, H. Wang, D. Dang, B. Chi, H. Liu, E.J. M. Hensen, X.W. Lou, B.Y. Xia, Engineering bunched Pt-Ni alloy nanocages for efficient oxygen reduction in practical fuel cells, Science 366 (2019) 850–856.
[34] J.R. Kitchin, J.K. Norskov, M.A. Barteau, J.G. Chen, Modification of the surface electronic and chemical properties of Pt(111) by subsurface 3d transition metals, J. Chem. Phys. 120 (2004) 10240–10246.

[35] M. Mavrikakis, B. Hammer, J.K. Norskov, Effect of strain on the reactivity of metal surfaces, Phys. Rev. Lett. 81 (1998) 2819–2822.
[36] V.R. Stamenkovic, B. Fowler, B.S. Mun, G.F. Wang, P.N. Ross, C.A. Lucas, N. M. Markovic, Improved oxygen reduction activity on Pt3Ni(111) via increased surface site availability, Science 315 (2007) 493–497.
[37] P. Hernandez-Fernandez, F. Masini, D.N. McCarthy, C.E. Strebel, D. Friebel, D. Deiana, P. Malacrida, A. Nierhoff, A. Bodin, A.M. Wise, J.H. Nielsen, T. W. Hansen, A. Nilsson, I.E.L. Stephens, I. Chorkendorff, Mass-selected nanoparticles of PtxY as model catalysts for oxygen electroreduction, Nat. Chem. 6 (2014) 732–738.
[38] M. Escudero-Escribano, P. Malacrida, M.H. Hansen, U.G. Vej-Hansen, A. Velázquez-Palenzuela, V. Tripkovic, J. Schiøtz, J. Rossmeisl, I.E.L. Stephens, I. Chorkendorff, Tuning the activity of Pt alloy electrocatalysts by means of the lanthanide contraction, Science 352 (2016) 73–76.
[39] I.E.L. Stephens, A.S. Bondarenko, U. Gronbjerg, J. Rossmeisl, I. Chorkendorff, Understanding the electrocatalysis of oxygen reduction on platinum and its alloys, Energ. Environ. Sci. 5 (2012) 6744–6762.
[40] J. Li, S. Sharma, X. Liu, Y.-T. Pan, J.S. Spendelow, M. Chi, Y. Jia, P. Zhang, D. A. Cullen, Z. Xi, H. Lin, Z. Yin, B. Shen, M. Muzzio, C. Yu, Y.S. Kim, A.A. Peterson, K.L. More, H. Zhu, S. Sun, Hard-Magnet L10-CoPt nanoparticles advance fuel cell catalysis, Joule 3 (2019) 124–135.
[41] N.N. Kariuki, D.J. Myers, Impact of nickel ions on the oxygen reduction reaction kinetics of Pt and on oxygen diffusion through ionomer thin films, J. Electrochem. Soc. 168 (2021), 064505.
[42] N. Ramaswamy, S. Kumaraguru, W. Gu, R.S. Kukreja, K. Yu, D. Groom, P. Ferreira, High-current density durability of Pt/C and PtCo/C catalysts at similar particle sizes in PEMFCs, J. Electrochem. Soc. 168 (2021), 024519.
[43] A. Kongkanand, M.F. Mathias, The priority and challenge of high-power performance of low-platinum proton-exchange membrane fuel cells, J. Phys. Chem. Lett. 7 (2016) 1127–1137.
[44] T.A. Greszler, D. Caulk, P. Sinha, The impact of platinum loading on oxygen transport resistance, J. Electrochem. Soc. 159 (2012) F831.
[45] C.Y. Ahn, J.E. Park, S. Kim, O.H. Kim, W. Hwang, M. Her, S.Y. Kang, S. Park, O. J. Kwon, H.S. Park, Y.H. Cho, Y.E. Sung, Differences in the electrochemical performance of Pt-based catalysts used for polymer electrolyte membrane fuel cells in liquid half- and full-cells, Chem. Rev. 121 (2021) 15075–15140.